NRC·CNRC

NRC Publications Archive
Archives des publications du CNRC

Probing Ca^{2+}-induced conformational change of calmodulin with gold nanoparticle-decorated single-walled carbon nanotube field-effect transistors

Shao, Wenting; Burkert, Seth C.; White, David L.; Scott, Valerie L.; Ding, Jianfu; Li, Zhao; Ouyang, Jianying; Lapointe, François; Malenfant, Patrick R. L.; Islam, Kabirul; Star, Alexander

This publication could be one of several versions: author's original, accepted manuscript or the publisher's version. / La version de cette publication peut être l'une des suivantes : la version prépublication de l'auteur, la version acceptée du manuscrit ou la version de l'éditeur.
For the publisher's version, please access the DOI link below./ Pour consulter la version de l'éditeur, utilisez le lien DOI ci-dessous.

Publisher's version / Version de l'éditeur:
https://doi.org/10.1039/C9NR03132D
Nanoscale, 11, 28, pp. 13397-13406, 2019-07-18

NRC Publications Archive Record / Notice des Archives des publications du CNRC :
https://nrc-publications.canada.ca/eng/view/object/?id=b39b6e61-a4c9-4026-9781-394d04fe6fee
https://publications-cnrc.canada.ca/fra/voir/objet/?id=b39b6e61-a4c9-4026-9781-394d04fe6fee

Access and use of this website and the material on it are subject to the Terms and Conditions set forth at
https://nrc-publications.canada.ca/eng/copyright
READ THESE TERMS AND CONDITIONS CAREFULLY BEFORE USING THIS WEBSITE.

L'accès à ce site Web et l'utilisation de son contenu sont assujettis aux conditions présentées dans le site
https://publications-cnrc.canada.ca/fra/droits
LISEZ CES CONDITIONS ATTENTIVEMENT AVANT D'UTILISER CE SITE WEB.

Questions? Contact the NRC Publications Archive team at PublicationsArchive-ArchivesPublications@nrc-cnrc.gc.ca. If you wish to email the authors directly, please see the first page of the publication for their contact information.

Vous avez des questions? Nous pouvons vous aider. Pour communiquer directement avec un auteur, consultez la première page de la revue dans laquelle son article a été publié afin de trouver ses coordonnées. Si vous n'arrivez pas à les repérer, communiquez avec nous à PublicationsArchive-ArchivesPublications@nrc-cnrc.gc.ca.

National Research Council Canada | Conseil national de recherches Canada

Canada

Nanoscale

Probing Ca2+-induced conformational change of Calmodulin with gold nanoparticle-decorated single-walled carbon nanotube field-effect transistors

Journal:	*Nanoscale*
Manuscript ID	NR-ART-04-2019-003132.R1
Article Type:	Paper
Date Submitted by the Author:	20-Jun-2019
Complete List of Authors:	Shao, Wenting; University of Pittsburgh, Department of Chemistry Burkert, Seth C.; University of Pittsburgh, Department of Chemistry White, David ; University of Pittsburgh, Department of Chemistry Scott, Valerie; University of Pittsburgh, Department of Chemistry Ding, Jianfu; National Research Council Canada, Institute for Chemical Process and Environmental Technology Li, Zhao; National Research Council Canada, Institute for Chemical Process and Environmental Technology Ouyang, Jianying; National Research Council Canada, Security and Disruptive Technologies Portfolio Lapointe, François; National Research Council Canada, Security and Disruptive Technologies Portfolio Malenfant, Patrick; NRC, SDT Islam, Kabirul; University of Pittsburgh, Chemistry Star, Alexander; University of Pittsburgh, Department of Chemistry

SCHOLARONE™
Manuscripts

Probing Ca^{2+}-induced conformational change of Calmodulin with gold nanoparticle-decorated single-walled carbon nanotube field-effect transistors

Wenting Shao[†], Seth C. Burkert[†], David L. White[†], Valerie L. Scott[†], Jianfu Ding[‡], Zhao Li[‡], Jianying Ouyang[‡], Francois Lapointe[‡], Patrick R. L. Malenfant[‡], Kabirul Islam[†], Alexander Star[†]*

[†] Department of Chemistry, University of Pittsburgh, Pittsburgh, Pennsylvania 15260, United States

[‡] Security and Disruptive Technologies Portfolio, National Research Council Canada, 1200 Montreal Road, Ottawa, Ontario, K1A 0R6, Canada

ABSTRACT: Nanomaterials are ideal for electrochemical biosensors, with their nanoscale dimensions enabling the sensitive probing of biomolecular interactions. In this study, we compare field-effect transistors (FET) comprised of unsorted (un-) and semiconducting-enriched (sc-) single-walled carbon nanotubes (SWCNTs). un-SWCNTs have both metallic and semiconducting SWCNTs in the ensemble, while sc-SWCNTs have a >99.9% purity of semiconducting nanotubes. Both SWCNT FET devices were decorated with gold nanoparticles (AuNPs) and were then employed in investigating the Ca^{2+}-induced conformational change of calmodulin (CaM) – a vital process in calcium signal transduction in the human body. Different biosensing behavior was observed from FET characteristics of the two types of SWCNTs, with sc-SWCNT FET devices displaying better sensing performance with a dynamic range from 10^{-15} M to 10^{-13} M Ca^{2+}, and a lower limit of detection at 10^{-15} M Ca^{2+}.

INTRODUCTION

Single-walled carbon nanotubes (SWCNTs) are considered to be an ideal material for electronic devices, such as field-effect transistors (FETs), due to their outstanding electronic and mechanical properties.[1-7] The properties of SWCNTs are largely dependent on their structure, therefore the control of SWCNT structure, such as diameter and chirality, is crucial for developing high-performance electronic devices.[7, 8] Unsorted (un-) SWCNTs contain a mixture of metallic (m-) and semiconducting (sc-) SWCNTs.[9] However, in order to achieve high-performance FET devices with high carrier mobility and high on/off ratios, a high purity of sc-SWCNTs is often required.[8, 10] Common methods for separating m-SWCNTs from sc-SWCNTs, include density gradient ultracentrifugation (DGU),[11] aqueous two-phase separation (ATP),[12] and conjugated polymer extraction (CPE).[13, 14] Among these methods, a hybrid-CPE protocol has been reported to yield sc-SWCNTs with a purity >99.9%.[15, 16] Recently, high-purity semiconducting SWCNTs have shown promise for chemical sensing applications, such as highly sensitive gas detection[17-19] and humidity monitoring.[20] The high sensitivity afforded by sc-SWCNT FETs seen in gas sensing could also be employed in the development of ultrasensitive biosensors, such as aptasensors[21, 22] and label-free protein sensors.[23, 24] In this paper, we applied high purity sc-SWCNT based FET devices to the investigation of the Ca^{2+} binding-induced conformational change of calmodulin (CaM).

CaM is a calcium binding messenger protein that modulates calcium transfer in many crucial processes in the human body, and ultimately modulates a variety of cellular processes.[25, 26] CaM is a ubiquitous, multifunctional protein that regulates over 30 different proteins and enzymes. As a highly conserved protein, CaM consists of only 148 amino acids, has a length of 65 Å, and a diameter of approximately 30 Å.[27] The small dimensions make CaM a suitable biological species to study on a carbon nanotube FET device because the conformational change of CaM can be monitored without being adversely affected by ionic screening effects when measured in relatively low ionic strength solutions. One interesting feature of the Ca^{2+}-induced conformational change of CaM is that, upon Ca^{2+} binding, CaM changes from a closed to an

open form, exposing the solvent accessible hydrophobic surface, which enables the recognition and binding of CaM to its target protein.[28] Therefore the conformational change of CaM plays a vital role in calcium signal transduction in the human body. Moreover, understanding of CaM structure could allow for the development of better protein conformational switches with applications in biosensors, diagnostic tools, and therapeutic agents.[29] Nuclear magnetic resonance (NMR) spectroscopy[28] and X-ray crystallography[30] are the primary techniques to study the protein conformational change, but these powerful instrumental methods have a limited miniaturization potential. Other methods such as fluorescence resonance energy transfer (FRET),[31] DNA nanolevers,[32] and atomic force microscopy (AFM)[33] have the advantage of single-molecule detection, however often require complex sample preparation such as protein labeling.

FET devices comprised of individual SWCNTs have already been used for real-time monitoring of biomolecular processes on the surface of SWCNTs, including single-molecule lysozyme dynamics[34] and the conformational dynamics of individual DNA G-quadruplex structures.[35] However, these approaches necessitate e-beam lithography and covalent attachment of biomolecules to nanotube sidewalls through patterning or point-defects. Herein, by utilizing networks of sc-SWCNT based FET devices, we detected the calcium ion-dependent conformational change of CaM without further modification of the protein or nanotubes. We measured FET characteristics to investigate steady state changes associated with ion-induced protein conformational changes and to explore the sensing performance and mechanism of sc-SWCNT FETs.

By comparing un-SWCNT and sc-SWCNT based FET devices, we further investigated effects of nanotube structure and functionalization on the biosensing performance. Purified arc-discharge un-SWCNTs have an unmodified graphitic surface but contain a mixture of m-SWCNTs and sc-SWCNTs, whereas semiconductor enriched sc-SWCNTs have a polyfluorene-dodecyl (PFDD) polymer coating due to the sorting process. Additionally, polymer coating in sc-SWCNTs can affect AuNP deposition and CaM binding in comparison to un-SWCNTs, which in turn can change biosensor performance. In addition to investigating FET transfer characteristics, we used ultraviolet-visible-near-infrared (UV-vis-NIR)

absorption and Raman spectroscopies to get additional insight into the electronic structure of the nanotube-gold nanoparticle-protein system.

EXPERIMENTAL METHODS

Carbon nanotube materials. Commercial unsorted single-walled carbon nanotubes (P2-SWNT, Carbon Solutions Inc.) and semiconducting single-walled carbon nanotubes were prepared according to reference 15 but may also be obtained commercially (IsoSol-S100, Raymor Industries Inc.).

Device fabrication and decoration with gold nanoparticles. Interdigitated gold electrodes (channel length of 10 μm) were patterned on a Si/SiO_2 substrate using photolithography. Un-SWCNT solution was prepared at 0.01 mg/mL in DMF, and sc-SWCNT solution was prepared at 0.05 mg/mL in toluene. SWCNTs were then deposited between gold electrodes via dielectrophoresis (DEP) with an ac frequency of 10 MHz for un-SWCNT, and 100 kHz for sc-SWCNT, applied bias voltage of 10 V, and bias duration of 60 s for un-SWCNT and 120 s for sc-SWCNT. Gold nanoparticle decoration on SWCNTs was achieved through bulk electrolysis from a 1 mM $AuCl_3$ solution in 0.1 M HCl using a 3-electrode system with a 1 M Ag/AgCl reference electrode, Pt counter electrode, and SWCNTs acting as the working electrode. A – 0.2 V potential was applied for 30 s for formation of AuNPs ranging in diameter from 10 nm to 100 nm.

Calmodulin (CaM) was functionalized to the AuNPs decorated SWCNTs by a 12-hour incubation with 50 μL of a 500 μg/mL CaM solution in 1 mM phosphate buffered saline (PBS) on the devices, followed by thorough rinsing with nanopure water.

FET measurements. FET characteristics of both un- and sc-SWCNT FET devices were studied employing liquid-gated FET device configuration. 0.01X Dulbecco's phosphate buffered saline (DPBS, Lonza) was used as the gating electrolyte. Characteristic FET curves, i.e., source-drain conductance (G) versus gate voltage (V_g), were taken by sweeping the gate voltage from +0.6 to – 0.6 V_g *versus* a 1 M Ag/AgCl reference electrode with a fixed source-drain voltage of 50 mV.

Raman measurements. XplorA Raman-AFM/TERS system was used to record all Raman spectra. Raman spectra were recorded using 638 nm (24 mW) and 785 nm (100 mW) laser excitation operating at 1% power.

UV-vis-NIR adsorption spectra. UV-vis-NIR spectra were collected using a Perkin-Elmer Lambda 900 UV-vis-NIR spectrophotometer. Un-SWCNTs were spray casted on a 1" X 1" quartz slide using a commercial air gun (Iwata, Inc), and sc-SWCNTs were drop casted on a 1" X 1" quartz slide. AuNPs were deposited on both types of SWCNTs through bulk electrolysis from a 1 mM $AuCl_3$ solution in 0.1 M HCl using a 3-electrode system. Both slides were then incubated with CaM solution (500 μg/mL in 1 mM PBS) to allow CaM binding to the nanomaterial surfaces.

SEM characterization. SEM images were taken on an SEM ZEISS Sigma500 VP with an accelerating voltage of 3 kV. Devices were sputter coated with 8 nm palladium before SEM imaging to limit charging.

AFM. Bruker multimode 8 utilizing a Veeco Nanoscope IIIa controller in tapping mode was used to collect AFM data. AppNano ACST-SS probes having nominal radius of 1-2 nm were operated at a frequency of 160−225 kHz, an amplitude set point of 1.70−1.75 V, and a drive amplitude of 100−300 mV. Images were processed in Gywiddon.

Circular dichroism (CD) measurements. Circular dichroism spectra were recorded on an Olis circular dichroism spectrophotometer. 1.0 mm quartz cuvettes were used for all measurements. 0.1 mg/mL Ca^{2+} free CaM and 0.1 mg/mL CaM solutions containing 10^{-15} M, 10^{-12} M, 10^{-9} M, 10^{-6} M and 10^{-3} M Ca^{2+} were prepared for CD measurements.

Expression of EGFP-CaM: A plasmid for mammalian expression of histidine tagged EGFP-calmodulin (EGFP-CaM) was obtained from Addgene (Plasmid # 47602). Human embryonic kidney 293T (HEK293T) cells were cultured in a T150 Flask (Corning) in Dulbecco's Modified Eagle's Media (DMEM) media supplemented with 10% Fetal Bovine Serum (FBS) at 37°C with 5% CO_2. At 80% cellular confluency, 25 µg of plasmid and 62.5 µg lipofectamine were added to 1.75 mL Optimem media and

incubated at room temperature for 5 minutes, separately. Next, the tubes were combined and incubated for 20 minutes. This was added to the cells with fresh DMEM 10% FBS. The cells were grown for an additional 24 hours and collected. Cells were resuspended in 750 µL lysis buffer containing: 50 mM tris pH 8.0, 200 mM NaCl, 10% glycerol, 1 mM phenylmethylsulfonyl fluoride (PMSF), 0.1% triton X, 1x protease inhibitor (Pierce), and small amounts of DNase and lysozyme. Following a 10-minute incubation on ice, the cells were subjected to sonication at 100 mA for five 60 second pulses with a 30 second resting period in between. Samples were then centrifuged at 15,000 rpm for 10 minutes to pellet cell debris. The protein was then purified by HisPur Nickel-NTA resin (ThermoFisher). Ni-NTA resin was prepared by washing 100 µL of the slurry with 5 column volumes (CV) water followed by 5 CV wash buffer: 50 mM tris pH 8.0, 200 mM NaCl, 10% glycerol, 25 mM imidazole, 1x protease inhibitor, and 1 mM PMSF. The lysate was applied to the resin and gently mixed for 1 hour at 4°C. Next, the beads were washed with 20 CV wash buffer. 600 µL of elution buffer containing 50 mM tris pH 8.0, 200 mM NaCl, 400 mM Imidazole, 10% glycerol, and 1 mM PMSF was applied to the column in 100 µL aliquots. All elutions containing protein were combined and concentrated (Sartorius centrifugal concentrator). Protein was quantified via SDS-PAGE with BSA standards (Biorad).

Fluorescence imaging. Fluorescence images were obtained using an Olympus 1X81/1X2-UCB microscope. 20 µL of 1 µM EGFP-CaM (containing 0.5mM ethylene glycol-bis(β-aminoethyl ether)-N,N,N',N'-tetraacetic acid, EGTA) was incubated on Au-SWCNT surface at 4°C overnight, and rinsed with nanopure water. Fluorescence images were captured under excitation of 489 nm and 655 nm. 20 µL of 1 M $CaCl_2$ was then dropcasted on the device surface to induce the conformational change of EGFP-CaM. After rinsing the surface with nanopure water, fluorescence images were captured under the same excitation wavelengths.

RESULTS AND DISCUSSION

For all studies, carbon nanotubes were deposited using dielectrophoresis (DEP) between interdigitated gold electrodes on Si/SiO_2 wafers. AuNPs were then deposited from a solution of $AuCl_3$ via bulk electrolysis in a three-electrode system, resulting in AuNPs anchoring to the oxygen-containing defect sites on carbon nanotubes.[36, 37] CaM functionalization of AuNP decorated SWCNTs (Au-SWCNT) was performed by incubating the chip with 500 µg/mL CaM solution for 12 h at room temperature, followed by rinsing with nanopure (18.2 MΩ) water.

Scanning electron microscopy (SEM) was utilized to characterize the difference in surface morphology after CaM functionalization for both types of FET devices (Figure 1). Figure 1a and b show the morphology and distribution of AuNPs on un-SWCNT and sc-SWCNT, respectively. For both types of SWCNT, nanotube networks were deposited between fingers of interdigitated gold electrodes. The un-SWCNTs tended to form large bundles and rope-like structures while sc-SWCNTs, due to polymer coating on their surfaces, did not bundle and formed denser and more interconnected networks than un-SWCNTs (Figure S1). AuNPs anchored on defect sites of both types of SWCNTs, forming larger particles ($d = 126.3 \pm 34.1$ nm, $n = 55$) on un-SWCNTs and smaller particles ($d = 68.4 \pm 20.0$ nm, $n = 106$) on sc-SWCNTs (calculated from SEM images of Au-un-SWCNTs and Au-sc-SWCNTs, including 8 nm of palladium coating). A primary difference between AuNP deposition on un-SWCNTs (Figure 1a) and sc-SWCNTs (Figure 1b) is the denser AuNP formation in the former case. Higher density AuNP formation is promoted by more available anchoring sites present in the un-SWCNTs resulting in larger quantities of CaM binding to the surface (Figure 1c), while the polymer coating on sc-SWCNTs may limit the decoration with AuNPs leading to less CaM on the surface (Figure 1d). Based on the prior work, we estimate a 1:1 weight ratio of wrapping polymer to SWCNT in thin films, yet excellent thin film transistor performance indicates that tube-tube junctions are not significantly affected by the polymer.[38] This is consistent with fewer binding locations for AuNPs on the polymer wrapped sc-SWCNTs.

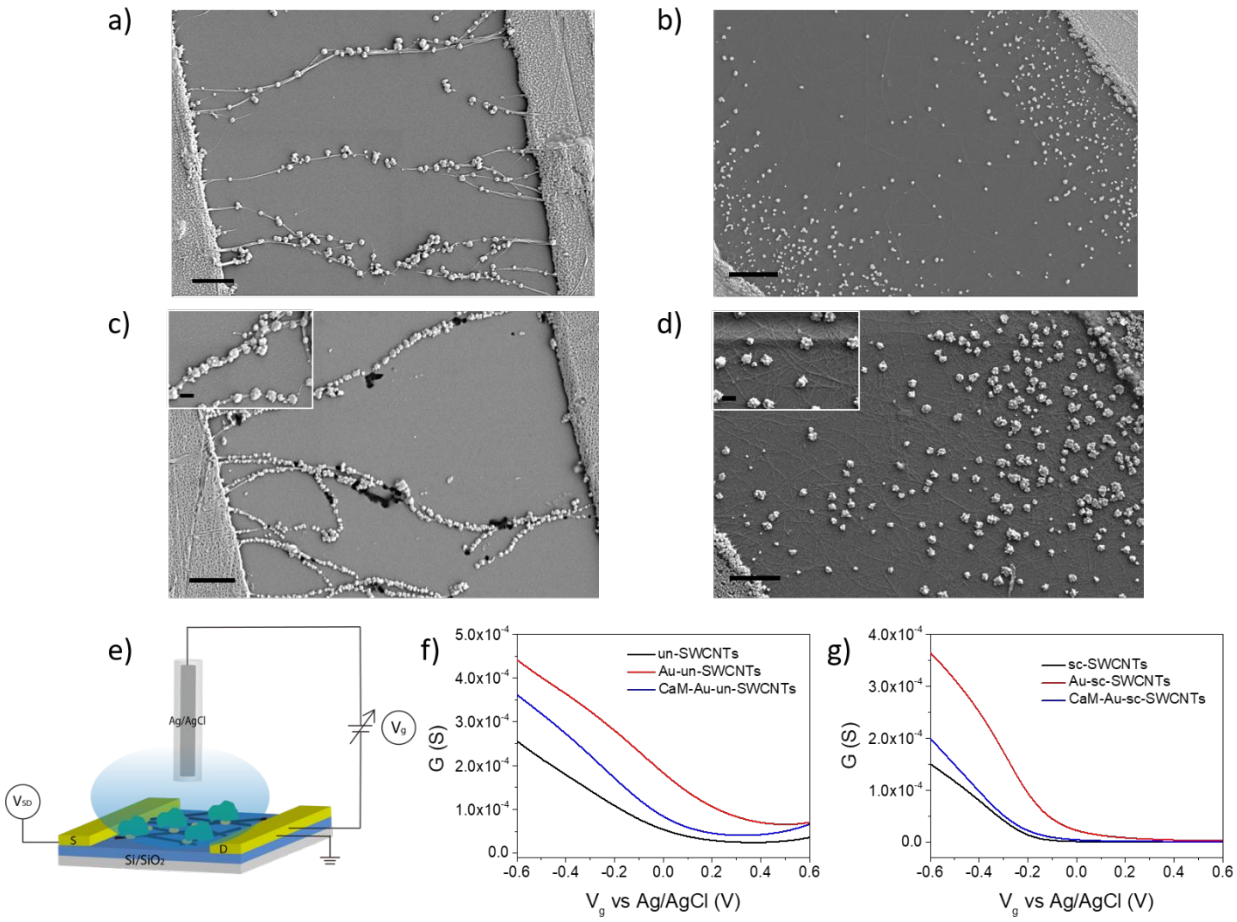

Figure 1 a-d) Scanning electron microscopy (SEM) images of AuNPs decorated un-SWCNT FET device (a) before and (c) after CaM binding, and AuNPs decorated sc-SWCNT (b) before and (d) after CaM binding. (Scale bar: 1 μm). Insets in panels c and d: zoom-in view of CaM covering AuNPs. (Scale bar: 200 nm). e) Schematic illustration of a liquid gated carbon nanotube FET. Interdigitated gold electrodes (yellow blocks) are configured as source (S) and drain (D) whereas gate voltage (V_g) is applied through a Ag/AgCl reference electrode. Source-drain bias (V_{SD}) is 50 mV. f-g) FET transfer characteristics, i.e., source-drain conductance (G) versus V_g, of (f) bare un-SWCNTs (black), Au-un-SWCNTs (red), and CaM-Au-un-SWCNTs (blue) and (g) bare sc-SWCNT (black), Au-sc-SWCNT (red), and CaM-Au-sc-SWCNT (blue).

Binding of CaM on AuNPs was confirmed by atomic force microscopy (AFM), which showed height profile change after CaM functionalization (Figure S2). CaM binds to AuNPs through gold-thiol bonds between its methionine (Met) residues and AuNPs. There are nine Met residues in CaM, with most of the

Met residues located at the hydrophobic target-binding surface. Met residues facilitate stabilization of the open conformation of CaM after Ca^{2+} binding and provide the target binding surface.[39] Therefore the Ca^{2+}-induced conformational change occurs near the surface of the device, and the change in FET transfer characteristics can be detected within the ionic screening length. A liquid-gated FET device configuration was employed to study the transfer characteristics of both types of SWCNT FET devices (Figure 1e). All liquid-gated measurements were carried out in 0.01 X DPBS where the Debye screening length is calculated to be 7.53 nm.[40] Figure 1f and 1g show typical transfer characteristics of p-type SWCNT FETs. Conductance of un-SWCNT FET devices in the ON state is consistent with what has been previously reported.[40, 41] The metallic component of un-SWCNTs contributes to the high conductance of un-SWCNT FET devices. Similar conductance was achieved for sc-SWCNT devices by using a relatively higher concentration of sc-SWCNTs during DEP process, forming dense networks across the channel. For both un-SWCNT and sc-SWCNT FET devices, AuNP decoration resulted in a significant increase in conductance. This observation can be attributed to the charge transfer from SWCNTs to AuNPs, which caused a depletion of electron density of the SWCNTs.[42] After the incubation with the CaM solution, the conductance decreased in the p-type region with more threshold voltage shifting to more negative values due to CaM binding onto the gold nanoparticles.

UV-vis-NIR absorption spectroscopy (Figure 2) provided complementary characterization of SWCNTs used in this study and revealed effects of functionalization on their electronic structure. UV-vis-NIR absorption spectra showed typical optical characteristics of SWCNTs associated with electronic transitions between van Hove singularities. For un-SWCNTs (Figure 2a), S_{11}, S_{22} and S_{33} peaks are characteristic of the semiconducting SWCNTs, whereas the metallic portion give rise to the M_{11} peaks from 600 nm to 800 nm. For sc-SWCNTs (Figure 2b), the S_{11}, S_{22} and S_{33} peaks are sharper with slight shifts to higher energies, indicating nanotube diameter selection after the extraction with PFDD polymer, whose presence can also be observed as a sharp peak at 392 nm. Additionally, the absence of M_{11} peaks confirms the high-purity semiconducting content in the sc-SWCNTs sample. During the functionalization of SWCNTs, the decrease

in the intensity of the S_{11} peak in both nanotube samples after AuNP decoration indicates the occurrence of charge transfer from SWCNTs to AuNPs during this process. However, AuNP-decorated un-SWCNTs (Figure 2a) showed more prominent absorption at 530 nm, which corresponds to the surface plasmon resonance (SPR) peak of AuNPs. After the incubation with the CaM solution, the increase in S_{11} peak of UV-vis-NIR spectra indicates an electron donation into SWCNTs after CaM binding. The AuNP SPR peak was less prominent in AuNP-decorated sc-SWCNTs (Figure 2b). This observation is consistent with SEM results that indicate smaller numbers of AuNPs were deposited on PFDD polymer-coated sc-SWCNTs as compared to un-SWCNTs (Figure S1). The smaller increase of S_{11} peaks after CaM binding is also consistent with smaller portion of AuNP-decorated sc-SWCNT available for CaM binding.

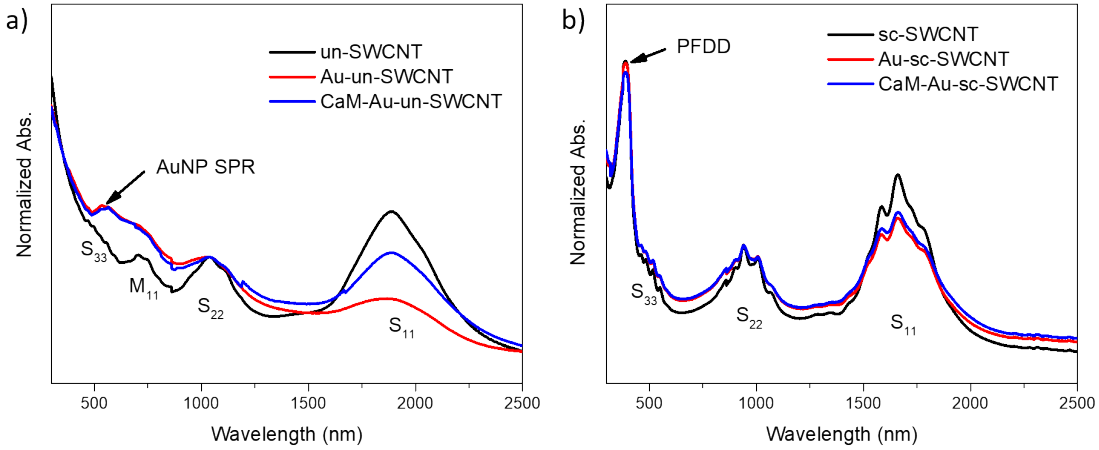

Figure 2 UV-vis-NIR absorption spectra of a) bare un-SWCNT (black), AuNPs decorated un-SWCNT (red) and CaM-functionalized Au-un-SWCNT (blue) and b) bare sc-SWCNT (black), AuNPs decorated sc-SWCNT (red) and CaM-functionalized Au-sc-SWCNT (blue).

Raman spectroscopy provided further evidence for characteristics of un- and sc-SWCNTs and the charge transfer process during functionalization. For all studies, Raman spectra were recorded using a 638 nm laser excitation. As shown in Figure 3, both Raman spectra show characteristic peaks of SWCNTs, i.e., RBM, D band, G band, and G' band. For un-SWCNTs (Figure 3a), the G band, ranging from 1400 cm^{-1} to 1700 cm^{-1}, is split into two peaks, G^+ peak and G^- peak, which are centered at 1587 cm^{-1} and 1550 cm^{-1}, respectively.

The broad and asymmetric G^- peak shown in Figure 3a has a Breit-Wigner-Fano (BWF) lineshape, which corresponds to the metallic feature of un-SWCNTs.[43] Similar to the Raman spectra of un-SWCNT, in the G band region of sc-SWCNTs from 1500 cm^{-1} to 1650 cm^{-1}, there are two peaks- G^+ peak centered around 1580 cm^{-1} and G^- peak centered around 1554 cm^{-1} (Figure 3b). However, in contrast to the broad G^- peak of un-SWCNT that has BWF lineshape, the G^- peak of sc-SWCNT is narrower with a Lorentzian lineshape, indicative of semiconducting carbon nanotubes.[15, 44] Radial breathing mode (RBM) peaks were characterized using a 785 nm laser excitation. Different RBM peak frequencies of un- and sc-SWCNTs under 785 nm laser excitation also confirms the high purity content of sc-SWCNTs (Figure S3).

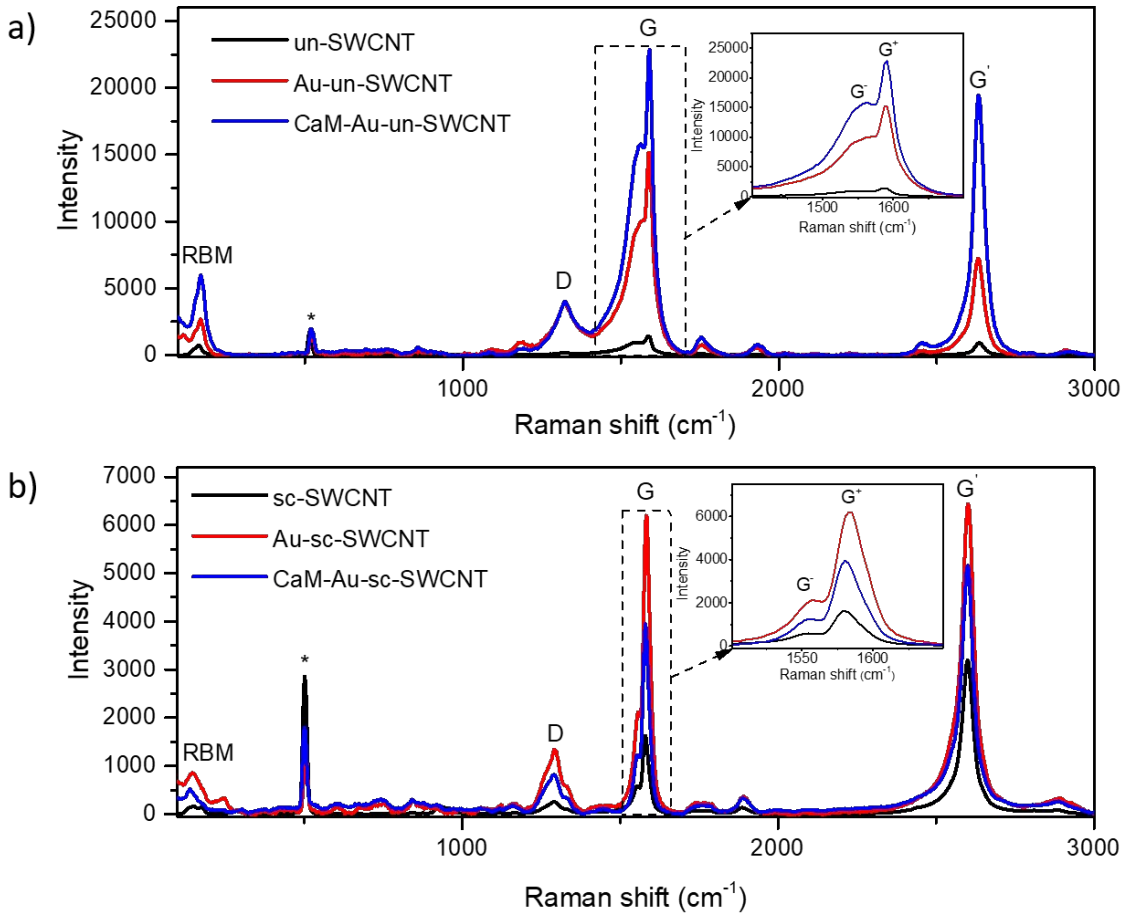

Figure 3 Raman spectra of a) bare un-SWCNT (black), AuNPs decorated un-SWCNT (red) and CaM-functionalized Au-un-SWCNT (blue) and b) sc-SWCNT (black), AuNPs decorated sc-SWCNT (red) and

CaM-functionalized Au-sc-SWCNT (blue). Insets show G region of un- and sc-SWCNT. The peaks labeled with asterisks are associated with silicon substrate.

Gold nanoparticle-decoration resulted in a 10.6 X and 3.8 X enhancement in G peak intensity for un-SWCNT and sc-SWCNT respectively, which is due to surface-enhanced Raman scattering (SERS) effect that arises from the excitation of surface plasmons on metal nanoparticles.[45] The larger enhancement of Raman intensities of un-SWCNTs corresponds to the larger quantities of AuNPs on un-SWCNTs. In addition to the enhancement effect, the G^+ peak of both types of SWCNTs experienced shifting toward higher energy (3.0 cm^{-1} for un-SWCNT and 3.3 cm^{-1} for sc-SWCNT). The blueshift of the G^+ peak suggests that the coupling between AuNPs and SWCNTs induced an electron transfer from SWCNTs to AuNPs, thus p-doping the SWCNTs, hardening the G^+ peak.[46, 47] This result is consistent with our conclusion from UV-vis-NIR absorption spectroscopy. Upon CaM binding, featured peaks from CaM are almost unnoticeable in the spectra.[25] Therefore, we use SWCNTs as a proxy chromophore to investigate the binding of CaM on Au-SWCNTs. A redshift from 1583 cm^{-1} to 1580 cm^{-1} of the G^+ peak of sc-SWCNTs was observed, indicative of electron transfer back to un-SWCNTs.[46] However, for un-SWCNTs, the charge donation mainly affected the metallic portion of un-SWCNTs, narrowing the G^- peak.[48]

The Ca^{2+}-induced conformational change of CaM was first studied in solution via circular dichroism (CD) spectroscopy. CD spectra of 0.1 mg/mL calcium-free CaM and 0.1 mg/mL CaM solutions containing 10^{-15} M to 10^{-3} M Ca^{2+} were recorded. Increase in the negative bands at 208 nm and 221 nm was observed due to the increase in α-helical content as more CaM changed from calcium-free to calcium-bound conformation (Figure S4).[49, 50] We further used enhanced green fluorescent protein fused calmodulin (EGFP-CaM) to confirm the conformational change of CaM on Au-SWCNT surfaces. EGFP-CaM was expressed from cells and purified (Figure S5). EGFP-CaM was functionalized on Au-SWCNT surfaces by incubating 2 μM EGFP-CaM solution on chip, and fluorescence images of the device surface were captured before and after addition of Ca^{2+}. An enhanced fluorescent signal between interdigitated gold electrodes

was observed under 489 nm excitation light (Figure 4). Previous studies of EGFP-CaM have shown that the conformational change of CaM can induce a structural perturbation of the GFP moiety, modulating its fluorescence activity, resulting in an increase in EGFP fluorescence upon Ca^{2+} binding to CaM.[51, 52] Therefore the enhancement of fluorescence suggests the occurrence of the Ca^{2+}-induced conformational change of CaM on the FET device surface.

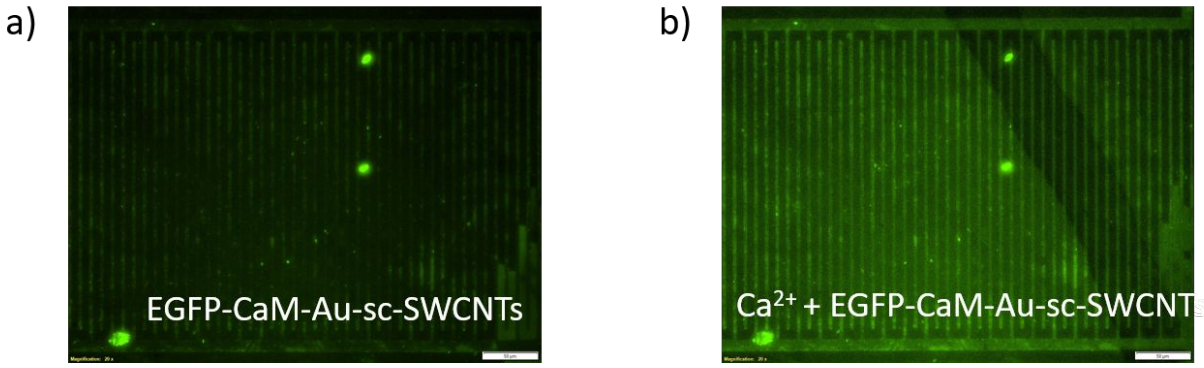

Figure 4 Fluorescence images of SWCNT FET device a) before and b) after Ca^{2+} binding.

To investigate the effect of Ca^{2+}-induced conformational change of CaM on carbon nanotube FET devices, liquid-gated FET measurements were performed with a 1 M Ag/AgCl electrode as the gate electrode. For each FET measurement, both nanotube devices were first incubated with $CaCl_2$ solution for 2 min, then rinsed with nanopure water, and measured in 0.01X PBS as the electrolyte medium with gate voltage sweeping from +0.6 V to -0.6 V. Measurement at constant ionic strength is important to eliminate any impact of different $CaCl_2$ salt concentrations on the Debye length and the measured signal of carbon nanotube FET devices.

Responses of CaM-Au-un-SWCNT FET devices were recorded in 0.01 X PBS after incubation in a series of Ca^{2+} solutions with concentrations from 10^{-11} M to 10^{-3} M. By plotting the source-drain conductance (G) vs. applied gate voltage (V_g), a consistent decrease in the overall conductance of the device with increasing concentrations of calcium ions was observed (Figure 5a). A calibration curve was

constructed by plotting the relative conductance change at – 0.5 V_g ($\Delta G/G_0$, where $\Delta G = |G_{-0.5V_g} - G_0|$, and G_0 is the conductance in buffer solution before Ca^{2+} exposure at -0.5 V_g) against concentrations of Ca^{2+} solution. The calibration curve was fit using a five-parameter logistic model[53], and the linear range of CaM-Au-un-SWCNT FET devices was determined to be 10^{-9} M to 10^{-7} M with a calibration sensitivity (m, defined as the slope of the linear region of the calibration curve) of 0.080 (Figure 5b). The FET transfer characteristics of CaM-Au-sc-SWCNT FET devices, on the other hand, showed a consistent shift towards more positive region in the threshold voltage with increasing concentration of Ca^{2+} (Figure 5c), and the linear range of the device was from 10^{-15} M to 10^{-13} M with a calibration sensitivity of 0.12 (Figure 5d). FET characteristics measured on different devices showed larger device-to-device variation for sc-SWCNT FET devices (Figure S6).

Control experiments were performed to prove that the sensitivity of the CaM-Au-SWCNT FET devices can be attributed to the conformational change of CaM. Figure 5e shows the calibration sensitivity of the active and control systems. The active system for both types of SWCNT FET devices have the best sensitivity in the corresponding dynamic range. Among control systems, both types of devices display sensitivity towards Ca^{2+} when having CaM on bare SWCNTs, but the sensitivity is significantly less than that of the active system which we attribute to reduced CaM present and random orientation of binding on the defect sites of SWCNTs (Figure S7). In the absence of CaM on the SWCNTs and Au-SWCNTs, the responses of both types of devices show minimal sensitivity or poor linearity towards different concentrations of Ca^{2+} due to the lack of conformational change of CaM (Figure S7). Additionally, the poor sensitivity of the active systems towards Mg^{2+}, an ion that induces less pronounced structural changes of CaM than Ca^{2+} does when bound to the protein,[54] provides further evidence that the sensitivity of the devices is a result of the conformational change of CaM. In the presence of bovine serum albumin (BSA), an interfering protein that has a calcium binding constant of ~90 M^{-1} in 0.01 X PBS buffer (3-4 orders of magnitude lower than that of CaM),[55] the active systems still show good sensitivity toward Ca^{2+} with 41% lost in calibration sensitivities for un-SWCNT devices and 27% for sc-SWCNT devices. However, it is demonstrated that the

devices are not sensitive toward BSA itself (Figure 5e). The loss in calibration sensitivity is likely due to the binding between Ca^{2+} and BSA, reducing the amount of CaM that undergoes the conformational change.

Gate leakage current in both types of devices was also analyzed to investigate whether or not encapsulating Au source and drain electrodes would affect the sensing performance. The results show (Figure S8) that the leakage current is insignificant compared with the measured source-drain current, therefore the effect of leakage current is negligible.

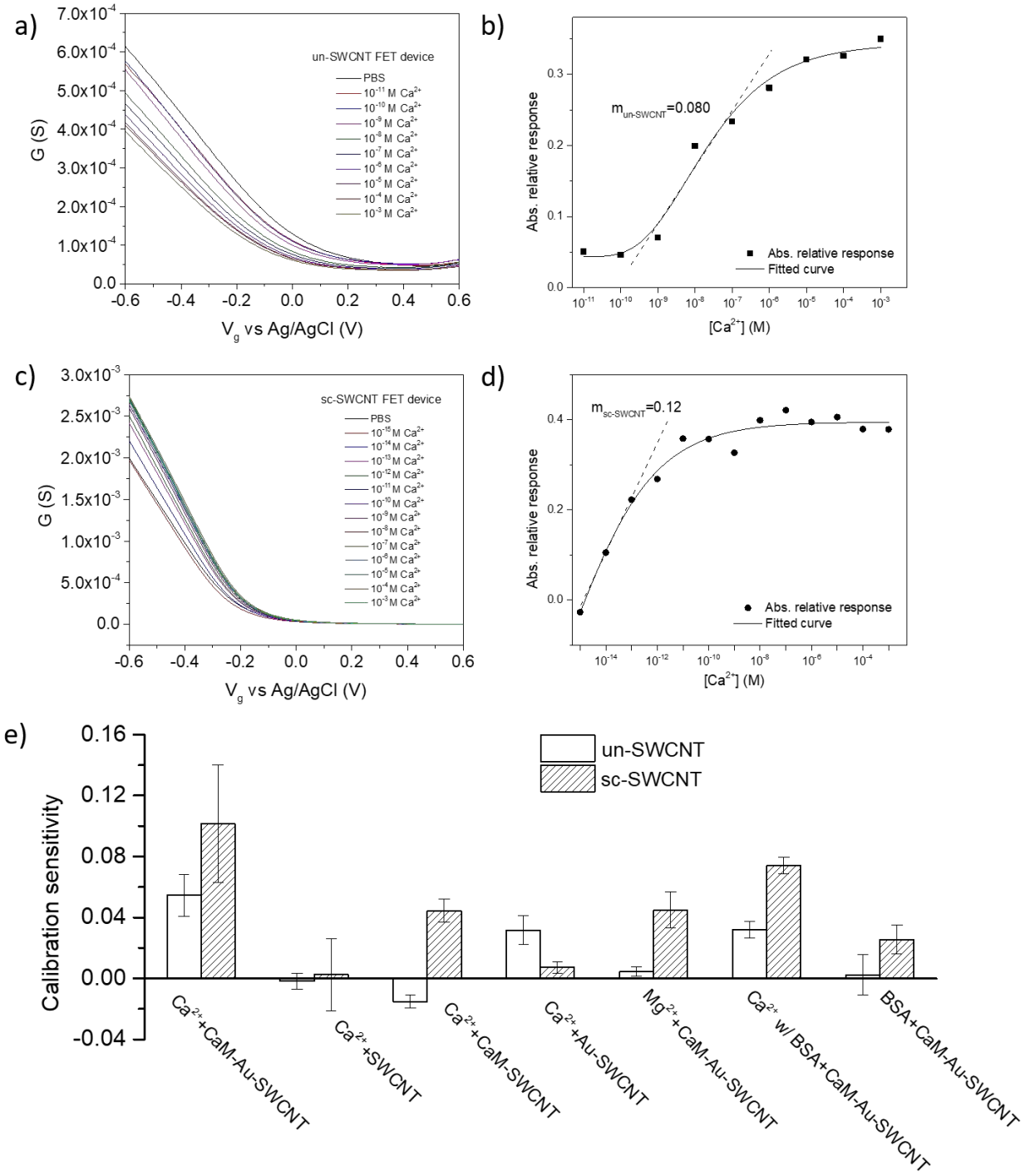

Figure 5 a) FET characteristic curves of un-SWCNT FET devices upon exposure to increasing concentrations of $CaCl_2$. b) Calibration plot for Ca^{2+} sensing with un-SWCNT FET devices. c) FET characteristic curves of sc-SWCNT FET devices with exposure to increasing concentrations of $CaCl_2$. d) Calibration plot for Ca^{2+} sensing with sc-SWCNT devices. e) Calibration sensitivity of the active system

and control systems for un- and sc-SWCNT FET devices. Calibration sensitivity is defined as the slope of the linear range. (Error bars are calculated from multiple devices).

For Au-un-SWCNT devices, the sensing mechanism behind the consistent drop in device conductance is attributed to the Schottky barrier effect. With the occurrence of conformational change at the SWCNT-AuNPs contact region, the local work function of metal is reduced, which leads to an alteration of the Schottky barrier of the nanotube-metal interfaces, therefore decreasing the conductance of the FET device.[56] This effect is further amplified by the presence of multiple nanoscale Schottky barriers formed across AuNP-nanotube interfaces.[57-58] However, the opposite shift of the FET characteristics of Au-sc-SWCNT devices suggests an alternative sensing mechanism due to the different properties between un-SWCNT and sc-SWCNT. Instead of Schottky barrier effect, the conformational change of CaM caused an exposure of its negatively charged side chains to the local environment,[59] inducing additional hole carriers in sc-SWCNTs, therefore shifting the I-Vg curves toward more positive gate voltages due to electrostatic gating effect.[60] This effect does not play a dominant role in un-SWCNT due to the presence of metallic SWCNTs and multiple interfaces between AuNP and SWCNTs. M-SWCNTs have constant density of state (DOS) near the Fermi level,[61] making them less sensitive to Fermi level shifts, and Schottky barrier modulation consequently overwhelms the doping effect on semiconducting nanotubes in un-SWCNTs.

Interestingly, the sc-SWCNT FET devices display a higher slope of the calibration curve and a linear range over lower Ca^{2+} concentrations when compared with un-SWCNT FET devices. The higher slope of the calibration curve can be attributed to the high on/off ratio of the transistor. In our case, the on/off ratio of un-SWCNT FET device is only ~3, whereas the on/off ratio of sc-SWCNT FET device is ~10^4 (Figure S9). Higher on/off ratio can lead to higher relative response, making the FET more sensitive to small shift in the threshold voltage, hence the better calibration sensitivity for sc-SWCNT FET devices (Figure S10). The high purity of semiconducting SWCNT contributes to the high on/off ratio of sc-SWCNT FET devices. In contrast, the presence of metallic SWCNTs in un-SWCNTs provides electrically conducting pathways, inhibiting the ability of the transistor to reach low off state conductance. However, sc-SWCNT FET devices saturated at lower concentrations of Ca^{2+} than un-SWCNT devices. The absolute relative conductance

change increased linearly with Ca^{2+} from 10^{-15} M to 10^{-13} M (in logarithmic scale), and then reached a plateau after 10^{-11} M, showing saturation of the devices (Figure 5d and Figure S6). This can be attributed to the limited amount of CaM detectable on sc-SWCNT devices. As mentioned earlier, AuNP deposition formed larger and denser AuNPs on un-SWCNTs than sc-SWCNTs, but the average size of CaM after binding to AuNPs on un-SWCNTs and sc-SWCNTs, 137.7 ± 37.4 nm (n = 45) and 155.2 ± 42.5 nm (n = 26) respectively (calculated from SEM images of CaM-Au-un-SWCNTs and CaM-Au-sc-SWCNTs, including 8 nm palladium coating), are relatively comparable considering the large standard deviation. This is indicative of more CaM aggregates on each AuNP on sc-SWCNTs due to limited binding sites for CaM. However, due to the limitation of Debye screening length, only the conformational change of CaM occurring at the SWCNT-AuNPs contact region can be probed. Therefore, with smaller AuNP surface area on sc-SWCNT devices, the amount of CaM detectable upon conformational change is reduced, making the sc-SWCNT FET devices saturate at lower concentration of Ca^{2+} than un-SWCNT devices.

Therefore, high-purity sc-SWCNTs FETs, besides their outstanding sensing performance towards small molecules such as hydrogen and ammonia gas, sensitively detect the change of charge distribution of CaM upon Ca^{2+}-induced conformational change with Ca^{2+} as low as 10^{-15} M. This low limit of detection indicates only 0.2 femtomolar CaM is required for the detection of the conformational change,[62] which significantly lowered the amount of CaM sample required by other techniques such as NMR[28] and X-ray crystallography.[30] Furthermore, with the limit of detection of 10^{-15} M Ca^{2+}, our CaM-functionalized Au-sc-SWCNT FET device can also function as a Ca^{2+} sensor that provides ultrasensitivity and selectivity when compared to other Ca^{2+} detection methods (Table S1).[63-66]

CONCLUSIONS

In summary, we compared FET responses of un- and sc-SWCNT FET devices during Ca^{2+}-induced conformational change of CaM. The sc-SWCNT FET devices exhibited better sensitivity towards the conformational change of CaM. The higher sensitivity can be attributed to the high on/off ratio of sc-

SWCNT FET devices, arising from the effective bandgap of high purity sc-SWCNT. The dynamic range at lower concentrations of Ca^{2+}, on the other hand, was due to the low CaM density on the device surface induced by the polymer wrapping on sc-SWCNT. Our SWCNT FET devices provide a label-free, highly sensitive and efficient way to probe the conformational change of CaM. To further improve our device for reliable and standardized sensing, controllable deposition and alignment of SWCNTs on FET devices are crucial. For example, uniform SWCNT networks can be formed in the channel by inkjet printing[38] or dip coating[67] for making thin-film transistors (TFTs) with <10% variability. We envision that our AuNPs-decorated high-purity semiconducting SWCNT FET devices can have further applications in detecting protein interactions.

ASSOCIATED CONTENT

Supporting Information:

Additional characterizations, sensing performance study and device reproducibility of un-SWCNT and sc-SWCNT FET devices, CD spectra of CaM and expression and purification of EGFP-CaM are available. This material is available free of charge via the internet at http://pubs.acs.org.

Corresponding author

*Email: astar@pitt.edu

Notes

The authors declare no competing financial interest.

ACKNOWLEDGEMENT

The XplorA Raman-AFM/TERS system was purchased via Defense University Research Instrumentation Program (DURIP) grant from the Office of Naval Research, ONR (N000141410765).

REFERENCES

1. R. H. Baughman, A. A. Zakhidov and W. A. d. Heer, *Science*, 2002, **297**, 787–792.
2. J. Li, H. T. Ng, A. Cassell, W. Fan, H. Chen, Q. Ye, J. Koehne, J. Han and M. Meyyappan, *Nano Lett.*, 2003, **3**, 597–602.
3. J. Koehne, H. Chen, J. Li, A. M. Cassell, Q. Ye, H. T. Ng, J. Han and M. Meyyappan, *Nanotechnology*, 2003, **14**, 1239–1245.
4. J. Li, Y. Lu, Q. Ye, M. Cinke, J. Han and M. Meyyappan, *Nano lett.*, 2003, **3**, 929–933.
5. J. E. Koehne, H. Chen, A. M. Cassell, Q. Ye, J. Han, M. Meyyappan and J. Li, *Clin. Chem.*, 2004, **50**, 1886–1893.
6. Y. Lu, J. Li, J. Han, H. T. Ng, C. Binder, C. Partridge and M. Meyyappan, *Chem. Phys. Lett.*, 2004, **391**, 344–348.
7. M. F. L. D. Volder, S. H. Tawfick, R. H. Baughman and A. J. Hart, *Science*, 2012, **339**, 535–539.
8. J. Lefebvre, J. Ding, Z. Li, P. Finnie, G. Lopinski and P. R. L. Malenfant, *Acc. Chem. Res.*, 2017, **50**, 2479–2486.
9. J. W. G. Wildoer, L. C. Venema, A. G. Rinzler, R. E. Smalley and C. Dekker, *Nature*, 1998, **391**, 59–62.
10. T. W. Odom, J.-L. Huang, P. Kim and C. M. Lieber, *Nature*, 1998, **391**, 62–64.
11. S. Ghosh, S. M. Bachilo and R. B. Weisman, *Nat. Nanotechnol.*, 2010, **5**, 443–450.
12. L. Wei, B. S. Flavel, W. Li, R. Krupke and Y. Chen, *Nanoscale*, 2017, **9**, 11640–11646.
13. F. Hennrich, W. Li, R. Fischer, S. Lebedkin, R. Krupke and M. M. Kappes, *ACS Nano*, 2016, **10**, 1888–1895.
14. V. Derenskyi, W. Gomulya, J. M. Rios, M. Fritsch, N. Frohlich, S. Jung, S. Allard, S. Z. Bisri, P. Gordiichuk, A. Herrmann, U. Scherf and M. A. Loi, *Adv. Mater.*, 2014, **26**, 5969–5975.
15. J. Ding, Z. Li, J. Lefebvre, F. Cheng, J. L. Dunford, P. R. Malenfant, J. Humes and J. Kroeger, *Nanoscale*, 2015, **7**, 15741–15747.
16. Z. Li, J. Ding, P. Finnie, J. Lefebvre, F. Cheng, C. T. Kingston and P. R. L. Malenfant, *Nano Res.*, 2015, **8**, 2179–2187.
17. M. Xiao, S. Liang, J. Han, D. Zhong, J. Liu, Z. Zhang and L. Peng, *ACS Sens.*, 2018, **3**, 749–756.
18. Z. Li, J. Ding, C. Guo, J. Lefebvre and P. R. L. Malenfant, *Adv. Funct. Mater.*, 2018, **28**, 1705568.
19. J. Y. Jeon, B. C. Kang, Y. T. Byun and T. J. Ha, *Nanoscale*, 2019, **11**, 1587–1594.
20. H. Zhang, L. Xiang, Y. Yang, M. Xiao, J. Han, L. Ding, Z. Zhang, Y. Hu and L. M. Peng, *ACS Nano*, 2018, **12**, 2773–2779.
21. H. Y. Zheng, O. A. Alsager, B. Zhu, J. Travas-Sejdic, J. M. Hodgkiss and N. O. Plank, *Nanoscale*, 2016, **8**, 13659–13668.
22. M. Thanihaichelvan, L. A. Browning, M. P. Dierkes, R. M. Reyes, A. V. Kralicek, C. Carraher, C. A. Marlow and N. O. V. Plank, *Biosens. Bioelectron.*, 2019, **130**, 408-413.
23. M. S. Filipiak, M. Rother, N. M. Andoy, A. C. Knudsen, S. Grimm, C. Bachran, L. K. Swee, J. Zaumseil and A. Tarasov, *Sens. Actuators B Chem.*, 2018, **255**, 1507–1516.
24. M. Hatada, T. T. Tran, W. Tsugawa, K. Sode and A. Mulchandani, *Biosens. Bioelectron.*, 2019, **129**, 254-259.
25. E. M. Jones, G. Balakrishnan, T. C. Squier and T. G. Spiro, *Protein Sci.*, 2014, **23**, 1094–1101.
26. C. F. Edman, S. E. George, A. R. Means, H. Schulman and P. Yaswen, *Eur. J. Biochem.*, 1994, **226**, 725–730.
27. R. H. Kretsinger, S. E. Rudnick and L. J. Weissman, *J. Inorg. Biochem.*, 1986, **28**, 289–302.
28. M. Zhang, T. Tanaka and M. Ikura, *Nat. Struct. Biol.*, 1995, **2**, 758–767.
29. A. J. DeGrave, J. H. Ha, S. N. Loh and L. T. Chong, *Nat. Commun.*, 2018, **9**, 1013–1021.

30. Y. S. Babu, C. E. Bugg and W. J. Cook, *J. Mol. Biol.*, 1988, **204**, 191–204.
31. H. Yuan, J. Qi, C. Xing, H. An, R. Niu, Y. Zhan, Y. Fan, W. Yan, R. Li, B. Wang and S. Wang, *Adv. Funct. Mater.*, 2015, **25**, 4412–4418.
32. A. Clery, T. J. M. Sohier, T. Welte, A. Langer and F. H. T. Allain, *Methods*, 2017, **118-119**, 137–145.
33. I. T. Li and G. C. Walker, *Proc Natl Acad Sci U S A*, 2011, **108**, 16527–16532.
34. Y. Choi, I. S. Moody, P. C. Sims, S. R. Hunt, B. L. Corso, I. Perez, G. A. Weiss and P. G. Collins, *Science*, 2012, **335**, 319–324.
35. D. Bouilly, J. Hon, N. S. Daly, S. Trocchia, S. Vernick, J. Yu, S. Warren, Y. Wu, R. L. Gonzalez, Jr., K. L. Shepard and C. Nuckolls, *Nano Lett.*, 2016, **16**, 4679–4685.
36. G. O. Silva, Z. P. Michael, L. Bian, G. V. Shurin, M. Mulato, M. R. Shurin and A. Star, *ACS Sens.*, 2017, **2**, 1128–1132.
37. Z. P. Michael, W. Shao, D. C. Sorescu, R. W. Euler, S. C. Burkert and A. Star, *J. Phys. Chem. C*, 2017, **121**, 20813–20820.
38. C. M. Homenick, R. James, G. P. Lopinski, J. Dunford, J. Sun, H. Park, Y. Jung, G. Cho and P. R. L. Malenfant, *ACS Appl. Mater. Interfaces*, 2016, **8**, 27900–27910.
39. E. M. Balog, L. E. Norton, D. D. Thomas and B. R. Fruen, *Am. J. Physiol. Heart Circ. Physiol.*, 2006, **290**, H794–H799.
40. A. M. Munzer, W. Seo, G. J. Morgan, Z. P. Michael, Y. Zhao, K. Melzer, G. Scarpa and A. Star, *J. Phys. Chem. C*, 2014, **118**, 17193–17199.
41. Y. Chen, H. Vedala, G. P. Kotchey, A. Audfray, S. Cecioni, A. Imberty, S. Vidal and A. Star, *ACS Nano*, 2012, **6**, 760–770.
42. D. R. Kauffman, D. C. Sorescu, D. P. Schofield, B. L. Allen, K. D. Jordan and A. Star, *Nano Lett.*, 2010, **10**, 958–963.
43. A. Jorio, C. Fantini, M. S. S. Dantas, M. A. Pimenta, A. G. Souza Filho, G. G. Samsonidze, V. W. Brar, G. Dresselhaus, M. S. Dresselhaus, A. K. Swan, M. S. Ünlü, B. B. Goldberg and R. Saito, *Phys. Rev. B*, 2002, **66**, 115411.
44. M. S. Dresselhaus, G. Dresselhaus, R. Saito and A. Jorio, *Phys. Rep.*, 2005, **409**, 47–99.
45. A. Sabur, M. Havel and Y. Gogotsi, *Journal of Raman Spectroscopy*, 2008, **39**, 61–67.
46. R. Voggu, C. S. Rout, A. D. Franklin, T. S. Fisher and C. N. R. Rao, *J. Phys. Chem. C*, 2008, **112**, 13053–13056.
47. J. L. Xu, R. X. Dai, Y. Xin, Y. L. Sun, X. Li, Y. X. Yu, L. Xiang, D. Xie, S. D. Wang and T. L. Ren, *Sci. Rep.*, 2017, **7**, 6751.
48. J. L. B. D. Svedruzic, T. J. M. Y.-H. Kim, P. W. King and M. J. Heben, *Dalton Trans.*, 2008, DOI: 10.1039/b805658g, 5501–5506.
49. P. Bayley, S. Martin and G. Jones, *FEBS lett.*, 1988, **238**, 61–66.
50. L. Settimo, S. Donnini, A. H. Juffer, R. W. Woody and O. Marin, *Biopolymers*, 2007, **88**, 373–385.
51. J. Nakai, M. Ohkura and K. Imoto, *Nat. Biotechnol.*, 2001, **19**, 137–141.
52. Q. Wang, B. Shui, M. I. Kotlikoff and H. Sondermann, *Structure*, 2008, **16**, 1817–1827.
53. R. A. Herman, P. N. Scherer and G. Shan, *J. Immunol. Methods*, 2008, **339**, 245–258.
54. Z. Grabarek, *Biochim. Biophys. Acta*, 2011, **1813**, 913–921.
55. N. Fogh–Andersen, *Clin. Chem.*, 1977, **23**, 2122–2128.
56. R. J. Chen, H. C. Choi, S. Bangsaruntip, E. Yenilmez, X. Tang, Q. Wang, Y.-L. Chang and H. Dai, *J. Am. Chem. Soc.*, 2004, **126**, 1563–1568.
57. D. R. Kauffman and A. Star, *Nano Lett.*, 2007, **7**, 1863–1868.
58. M. Ding, Y. Tang and A. Star, *J. Phys. Chem. Lett.*, 2013, **4**, 147–160.
59. I. Andre, T. Kesvatera, B. Jonsson, K. S. Akerfeldt and S. Linse, *Biophys. J.*, 2004, **87**, 1929–1938.

60. I. Heller, A. M. Janssens, J. Mannik, E. D. Minot, S. G. Lemay and C. Dekker, *Nano Lett.*, 2008, **8**, 591–595.
61. J. N. Tey, X. Ho and J. Wei, *Nanoscale Res. Lett.*, 2012, **7**, 548–554.
62. Y. Ogawa and M. Tanokura, *J. Biochem.*, 1984, **95**, 19–28.
63. T. Alizadeh, A. N. Shamkhali, Y. Hanifehpour and S. W. Joo, *New. J. Chem.*, 2016, **40**, 8479–8487.
64. C. Ocana, N. Abramova, A. Bratov, T. Lindfors and J. Bobacka, *Talanta*, 2018, **186**, 279–285.
65. M. Wu, S. Meng, Q. Wang, W. Si, W. Huang and X. Dong, *ACS Appl. Mater. Interfaces*, 2015, **7**, 21089–21094.
66. S. R. Ankireddy and J. Kim, *Sens. Actuators B Chem.*, 2018, **255**, 3425–3433.
67. Z. Li, J. Ding, J. Lefebvre and P. R. L. Malenfant, *Org. Electron.*, 2015, **26**, 15–19.

TOC graphic

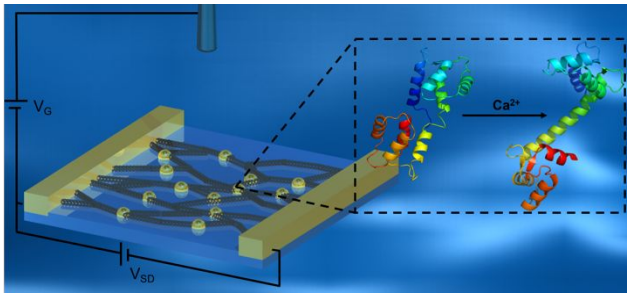

Nanoelectronic detection of ion-induced protein conformational changes with metal nanoparticle-decorated carbon nanotube FET.